Fermi arc mediated transport in an inversion symmetry broken Weyl semimetal nanowire and its hybrid junctions

Amartya Pal [1,2,*] Paramita Dutta [3,†] and Arijit Saha [1,2,‡]
[1]*Institute of Physics, Sachivalaya Marg, Bhubaneswar 751005, India*
[2]*Homi Bhabha National Institute, Training School Complex, Anushakti Nagar, Mumbai 400094, India*
[3]*Theoretical Physics Division, Physical Research Laboratory, Navrangpura, Ahmedabad 380009, India*

(Received 16 February 2024; revised 22 April 2024; accepted 4 June 2024; published 14 June 2024)

The emergence of gapless surface states, known as Fermi arcs (FAs), is one of the unique properties of the novel topological Weyl semimetal (WSM). However, extracting the signatures of FAs from the bulk states has always been a challenge as both of them are gapless in nature and connected to each other. We capture the signatures of FAs via transport in an inversion symmetry broken WSM. We study the band structure and the properties of FAs such as shape, and spin polarization considering slab and nanowire (NW) geometry, and then compute the two-terminal conductance in WSM NWs in terms of the scattering coefficients within the Landauer formalism. We find the FA-mediated conductance to be quantized in units of $2e^2/h$. We extend our study to transport in the WSM/Weyl superconductor NW hybrid junction using the Blonder-Tinkham-Klapwijk formalism. We show that due to the intricate spin textures, the signatures of the FAs can be captured via the Andreev reflection process. We also show that our results of conductance are robust against delta-correlated quenched disorder and thus enhance the experimental feasibility.

DOI: 10.1103/PhysRevB.109.235419

I. INTRODUCTION

Over the past decade, the Weyl semimetal (WSM) has emerged as a novel gapless topological phase in three-dimensional (3D) semimetals due to its nontrivial band structure and intriguing transport properties [1–5]. Weyl fermions were initially proposed as a solution to the massless Dirac equation in 1929 [6,7]. Later these fermions, as low-energy excitations, were theoretically proposed in 3D topological insulators at the transition phase between the trivial and nontrivial insulating phases by breaking either time reversal symmetry (TRS) or inversion symmetry (IS) [8,9], topological insulator heterostructures [10–15], pyrochlore iridates [16–18], etc. The experimental realizations of the WSM phase in real materials, e.g., TaAs, TaP, NbAs, NbP, WTe_2, magnetic Heusler materials, etc. [19–34], have opened up the opportunity for the plethora of research works for both theorists and experimentalists.

WSMs exhibit a unique bulk band structure where the valence and conduction bands intersect at an even number (minimum two for TRS-broken and four for IS-broken WSM) of isolated points in momentum space known as Weyl nodes (WNs). Around these WNs, the bulk bands disperse linearly with momentum, resembling the dispersion of 3D massless relativistic fermions. WNs are recognized as the monopoles of Berry curvature in momentum space, while their charge, termed chirality, determines their topological nature [1–5]. Importantly, WNs always appear pairwise with opposite chiralities, ensuring a net zero chiral charge over the entire Brillouin zone. Effects of both weak and strong disorder [35–39] and interactions [40–46] on the WSM phase have been investigated.

In addition to the nontrivial bulk bands, an intriguing and exotic aspect of WSMs is the presence of nontrivial surface states, known as Fermi arcs (FAs) [19–21,23–25,27,31,47–51]. When projected onto a surface Brillouin zone (sBZ), these surface states manifest as arcs with their end points located at the projection of the bulk WNs on the sBZ. Close to the projection of the WNs, FA states can leak into the bulk and reappear at the opposite sBZ [1–3]. Notably, both surface and bulk states of WSMs are gapless. This is in sharp contrast to the 3D topological insulators, where gapless surface states lie within the bulk gap and are exponentially localized near the surface. Signatures of these FAs in transport properties have been investigated both theoretically [52–57] and experimentally [28,49–51].

Due to the gapless nature, separating these surface states from the bulk and identifying the sole signatures of FAs in the transport measurement has always been a challenging task. Very recently, it has been shown that bulk states are gapped out in the TRS-broken WSM nanowire (NW) due to its finite-size effect. Within the bulk confinement gap, only surface states are present and their contributions to the conductance becomes quantized in units of e^2/h in a two-terminal setup [57]. However, most of the WSM phases in reality are observed to be IS broken (ISB) because of the plentitude of crystal structure asymmetries found in nature.

In recent years, investigation of transport properties in superconducting hybrid junctions of WSMs have attracted

*Contact author: amartya.pal@iopb.res.in
†Contact author: paramita@prl.res.in
‡Contact author: arijit@iopb.res.in

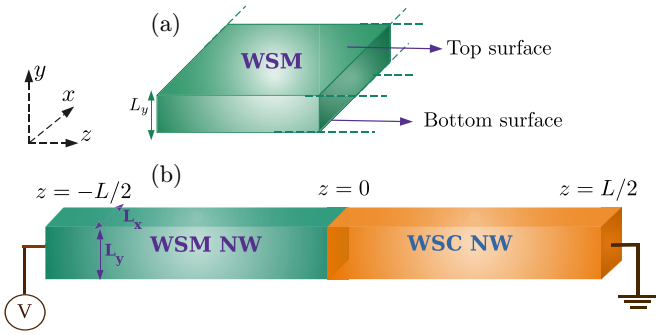

FIG. 1. (a) Schematic diagram of a WSM slab geometry with translational invariances along x and z directions, but a finite width (L_y) along y direction. (b) Schematic diagram of a WSM NW ($-L/2 < z < 0$)/WSC NW ($L/2 > z > 0$) hybrid junction in the presence of a voltage bias V, where L_x and L_y denote the finite sizes along x and y directions, respectively.

significant attention due to the interplay of superconductivity and the nontrivial topology of WSMs [58–67]. Most of these studies concern the bulk properties of WSM. Transport phenomena become much more subtle and fascinating when the role of surface states are also taken into account [68–74]. To date, there are a few studies on FA-mediated transport phenomena in the literature [57,75–78]. Particularly, signatures of FAs in ISB Weyl NW hybrid junctions have not been investigated so far in the literature, to the best of our knowledge. Since NW junctions are very useful in separating the contributions due to FAs, it remains interesting to look for the role of FAs in transport phenomena via the Andreev reflection (AR) in Weyl NW-based superconducting hybrid junctions.

With these motivations, in this present article, we investigate the ISB WSM NW in a two-terminal setup in two conditions: (i) the bare NW and (ii) its hybrid junction with superconducting pairing (WSC) tailoring a WSM/WSC NW junction as shown in Fig. 1. Here, superconductivity in WSC NW can be generated either via the proximity effect [68] or electron-electron correlation [59,69,79,80]. In our work, we address the following intriguing questions: (1) Is it possible to separate out the contributions of FAs from the bulk states in ISB WSM NW, similar to the TRS-broken WSM case? (2) Is it possible to capture the signature of FAs via the Andreev process in such hybrid junction? (3) Does the transport signature become quantized in ISB WSM junctions too? (4) Are these quantizations robust against disorder?

The rest of the article is organized as follows. In Sec. II, we introduce our model and compute and analyze the band structure and FAs in slab and NW geometry. In Sec. III, we investigate the conductance in WSM NW and WSM/WSC NW hybrid junctions, and subsequently in Sec. IV, we check the robustness of our results against the random on-site disorder. Finally, in Sec. V, we summarize and conclude our results.

II. MODEL AND BAND STRUCTURE

In this section, we first introduce our model of ISB WSM and WSM with superconducting correlation. For the discussion on the WSM phase in detail, we show the bulk band structure, followed by a thorough discussion on the surface states. To obtain the surface states, we require a finite boundary which can be achieved by making the WSM finite at least along one direction. For the sake of understanding the nature of surface states in detail, let us consider two different geometries: (i) the slab where it is finite along the y direction and (ii) NW where it is finite along both x and y directions. In both the slab and NW geometries, we analyze the locations of the FAs with their spin textures. For the NW geometry which is our main concern, we discuss the surface states in the WSM and WSC phases, with both the open boundary condition (OBC) and periodic boundary condition (PBC).

A. Model Hamiltonian

We consider an ISB WSM described by the second-quantized Hamiltonian on a cubic lattice with lattice spacing l (= 1) given by

$$\mathcal{H} = \sum_{\mathbf{k}} \psi_{\mathbf{k}}^{\dagger}\, \mathcal{H}_{\rm WSM}(\mathbf{k})\, \psi_{\mathbf{k}}, \tag{1}$$

where $\psi_{\mathbf{k}} = (c_{\mathbf{k},A,\uparrow}, c_{\mathbf{k},B,\uparrow}, c_{\mathbf{k},A,\downarrow}, c_{\mathbf{k},B,\downarrow})^T$ and $c_{\mathbf{k},\alpha,\sigma}$ ($c^{\dagger}_{\mathbf{k},\alpha,\sigma}$) represents the annihilation (creation) operator for an electron in the orbital α (= A, B) and spin $\sigma = (\uparrow, \downarrow)$. The momentum, $\mathbf{k}$ (= $\{k_x, k_y, k_z\}$), runs over the first BZ. Here, $\mathcal{H}_{\rm WSM}(\mathbf{k})$ is described by the four-band model as [64,65,81]

$$\mathcal{H}_{\rm WSM}(\mathbf{k}) = \lambda_x \sin k_x \tau_1 s_3 + \lambda_y \sin k_y \tau_2 s_0 + \beta \tau_2 s_2 + \alpha \sin k_y \tau_1 s_2 + \left[(m - 4t) + 2t \sum_{j=x,y,z} \cos k_j \right] \tau_3 s_0, \tag{2}$$

where $\lambda_{x,y}$ and t represent the spin-orbit coupling and nearest-neighbor hopping amplitudes, respectively, m is the crystal-field splitting energy, and β, α are the real parameters of the model. The Pauli matrices τ_i and s_i for $i \in \{0, 1, 2, 3\}$ act on the orbital and spin degrees of freedom of the electron, respectively. The term $\beta\tau_2 s_2$ in Eq. (2) is responsible for the breaking of IS, whereas the TRS is preserved following the conditions $\mathcal{P}^{\dagger}\mathcal{H}_{\rm WSM}(\mathbf{k})\mathcal{P} \neq \mathcal{H}_{\rm WSM}(-\mathbf{k})$ and $\mathcal{T}^{\dagger}\mathcal{H}_{\rm WSM}(\mathbf{k})\mathcal{T} = \mathcal{H}_{\rm WSM}(-\mathbf{k})$ where $\mathcal{P} = \tau_3 s_0$ and $\mathcal{T} = is_2\mathcal{K}$, with $\mathcal{K}$ being the complex conjugation operator. After diagonalization of the Hamiltonian in Eq. (2), the eigenvalues for $\mathcal{H}_{\rm WSM}$ are obtained as

$$E^2(\mathbf{k}) = [\sqrt{\sin^2 k_x + \sin^2 k_y} \pm \beta]^2 + (\alpha \sin k_y)^2 + \left(m - 4t + 2t \sum_{j=x,y,z} \cos k_j \right)^2. \tag{3}$$

Broken IS leads to four bulk WNs Q_s ($s = 1, 2, 3, 4$) located at $(\pm k_x^0, 0, \pm k_z^0)$, with $k_x^0 = \sin^{-1}(\beta)$ and $k_z^0 = \cos^{-1}(1 - \sqrt{1-\beta^2} - \frac{m}{2t})$ as depicted in Figs. 2(a) and 2(b). The presence of TRS implies that the WNs must appear in Kramer pairs (KPs) [1,2]. In our model, Q_1, Q_3 and Q_2, Q_4 form these KPs. TRS also ensures that WNs within a KP share the same chirality. Consequently, the overall chirality of the

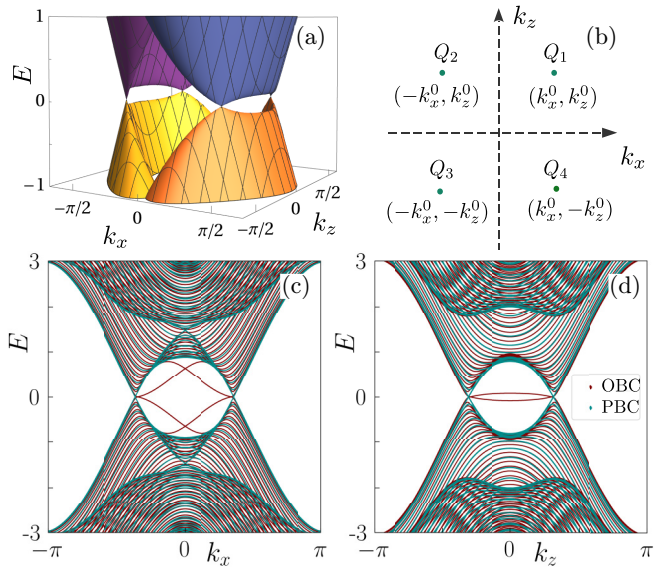

FIG. 2. (a) Bulk band structure of the ISB WSM is depicted in the $k_y = 0$ plane. (b) Locations of the four WNs are shown in the k_x-k_z plane choosing $k_y = 0$. (c), (d) Band structure of WSM considering slab geometry is demonstrated choosing $L_y = 40$ and considering both OBC and PBC along y direction.

system remains zero. Following that, the chiralities of Q_2, Q_4 are opposite to those of Q_1, Q_3.

For the superconducting part of the Hamiltonian, we consider s-wave spin-singlet intraorbital pairing which couples the electrons and holes between the WNs with same chirality, i.e., between Q_1, Q_3 and Q_2, Q_4 [63–65]. With this consideration, the Bogoliubov–de Gennes (BdG) Hamiltonian for the WSC part can be written as

$$\mathcal{H}_{\rm BdG} = (1/2)\sum_{\mathbf{k}} \Psi_{\mathbf{k}}^{\dagger}\mathcal{H}_{\rm WSC}(\mathbf{k})\Psi_{\mathbf{k}}, \tag{4}$$

where

$$\begin{aligned}\mathcal{H}_{\rm WSC}(\mathbf{k}) &= \lambda_x \sin k_x \tau_1 s_3 \pi_0 + \lambda_y \sin k_y \tau_2 s_0 \pi_3 + \beta \tau_2 s_2 \pi_3 \\ &+ \alpha \sin k_y \tau_1 s_2 \pi_3 + \Delta\, \tau_0 s_2 \pi_2 - \mu \tau_0 s_0 \pi_3 \\ &+ \left[(m - 4t) + 2t \sum_{j=x,y,z} \cos k_j\right] \tau_3 s_0 \pi_3, \end{aligned} \tag{5}$$

with $\Psi_{\mathbf{k}} = (c_{\mathbf{k},A,\uparrow}, c_{\mathbf{k},B,\uparrow}, c_{\mathbf{k},A,\downarrow}, c_{\mathbf{k},B,\downarrow}, c^{\dagger}_{-\mathbf{k},A,\uparrow}, c^{\dagger}_{-\mathbf{k},B,\uparrow}, c^{\dagger}_{-\mathbf{k},A,\downarrow}, c^{\dagger}_{-\mathbf{k},B,\downarrow})$ as the Nambu spinor. The Pauli matrices, π_i ($i = 0, 1, 2, 3$), act on the particle-hole degree of freedom. Here, Δ denotes the s-wave pairing potential and μ is the chemical potential measured with respect to Weyl nodes. For the rest of the article, we choose the following parameter values in our model: $\lambda_x = \lambda_y = 1$, $t = 1$, $\beta = 0.9$, $\alpha = 1.0$, $\mu = 0$, $m = 0$, $\Delta = 0.5$, and accordingly, we have $k_x^0 \simeq 1.11$ and $k_z^0 \simeq 0.97$. Note that the qualitative behavior of our results is not sensitive to the change in the parameter values as long as the WSM phase is preserved.

B. Slab geometry

With the discussions on the bulk properties, we now focus on the surface FA states in WSM. For that, we consider a slab geometry schematically shown in Fig. 1(a). Since the WNs are located in the k_x-k_z plane, we choose a slab to have a finite size along the y direction with thickness L_y such that the projection of all four WNs can be observed in the sBZ. Along the x and z directions, the WSM slab is infinite, so the momenta along these directions are still good quantum numbers. Consideration of the finite size along the y direction gives rise to two surfaces located at $y = 1$ (bottom surface) and $y = L_y$ (top surface) as shown Fig. 1(a).

Since the momentum along the y direction is not well defined, to find the band structure in slab geometry we first obtain the real-space Hamiltonian by performing an inverse Fourier transformation (FT) only along the y direction using

$$\begin{aligned} c_{\mathbf{k},\alpha,\sigma} &= \frac{1}{\sqrt{L_y}} \sum_{y=1}^{L_y} e^{ik_y y} c_{k_x k_z y,\alpha,\sigma}, \\ \psi_{\mathbf{k}} &= \frac{1}{\sqrt{L_y}} \sum_{y=1}^{L_y} e^{ik_y y} \psi_{k_x k_z y}. \end{aligned} \tag{6}$$

With this transformation, the Hamiltonian takes the form

$$\mathcal{H}^{\rm slab} = \sum_{k_x k_z} \sum_{y,y'=1}^{L_y} \psi^{\dagger}_{k_x k_z y} \mathcal{H}^{\rm slab}_{\rm WSM}(k_x, k_z, y, y') \psi_{k_x k_z y'},$$

where

$$\begin{aligned}\mathcal{H}^{\rm slab}_{\rm WSM}(k_x, k_z, y, y') &= [\lambda_x \sin k_x \tau_1 s_3 + \beta \tau_2 s_2 + (m - 4t)\tau_0 s_0 \\ &+ 2t(\cos k_x + \cos k_z)\tau_3 s_0]\delta_{y,y'} \\ &+ [(\lambda_y/2i)\tau_2 s_0 + (\alpha/2i)\tau_1 s_2 + t\tau_3 s_0] \\ &\times \delta_{y,y'+1} + \text{H.c.} \end{aligned} \tag{7}$$

We numerically diagonalize the above Hamiltonian for each set of (k_x, k_z) values with $L_y = 40$ slices considering both OBC and PBC along the y direction. Note that surface states can be observed only in OBC, while PBC is employed to identify only the bulk states. We show the band structure as a function of k_x by setting $k_z = 0.9$ in Fig. 2(c). The choice of k_z can be made anywhere in between $[-k_z^0, k_z^0]$ since the surface states only appear in between the WNs with opposite chiralities. Similarly, we depict the band structure as a function of k_z with $k_x = 1$ in Fig. 2(d) employing both OBC and PBC along the y direction. In both figures, we observe the gapless dispersive FA surface states between the WNs when OBC is implemented.

Now, we investigate the shape of the FAs obtained in the WSM slab geometry. FAs are the open constant energy contours in the k_x-k_z plane residing at the boundary of the system. We fix the energy at $E = 0.08t$ (t sets the energy scale in the system) and draw the Fermi surface in Fig. 3(a). With the OBC, we observe the existence of four FAs denoted by FA_γ with $\gamma = 1, 2, 3, 4$. As expected, two FAs connect WNs with opposite chirality, i.e., FA_1 and FA_2 (FA_3 and FA_4) connect the WNs, Q_2 and Q_3 (Q_1 and Q_4). On top of FAs, we also show the Fermi surface in PBC, which only contains the bulk states around each WN as shown in Fig. 3(a) using

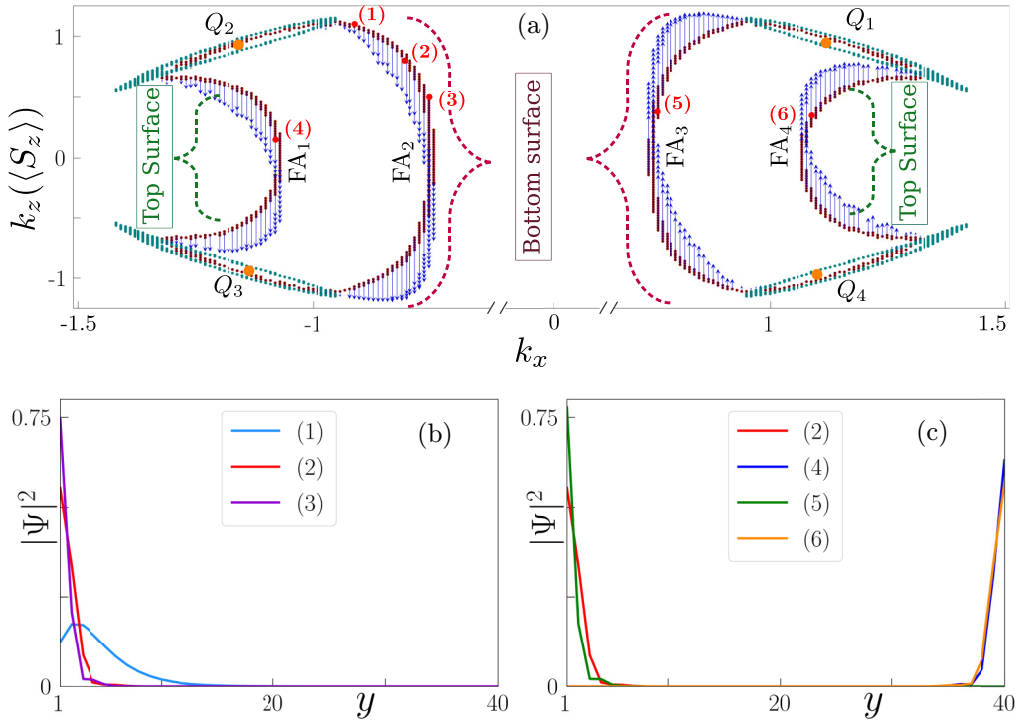

FIG. 3. (a) The features of Fermi arcs (FAs) (collection of brown points) for the ISB WSM, labeled as FA$_\gamma$ ($\gamma = 1, 2, 3, 4$) are depicted along with four WNs, Q_s ($s = 1, 2, 3, 4$) (orange color), in k_x-k_z plane considering slab geometry with $L_y = 40$ and $E = 0.08t$. Bulk Fermi surfaces are shown around each WN in teal color. The spin polarizations ($\langle S_z\rangle$ in the k_x-k_z plane) for the states on FAs are shown by blue arrows, where vertically upward (downward) arrows indicate the positive (negative) values of $\langle S_z\rangle$, respectively, with the length of each arrow being proportional to the magnitude of $\langle S_z\rangle$. (b), (c) $|\Psi|^2$ is illustrated as a function of position y for the six states [marked by red dots in panel (a)] to highlight their locations.

teal color. Interestingly, the shape of FAs obtained in this model closely resembles the FAs observed in real materials [20,21,23,25,31,33].

To get insight about the locations of the states on the FAs in real space, we depict $|\Psi|^2$ [$\equiv |\psi_{k_xk_z}(y)|^2$] as a function of y in Figs. 3(b) and 3(c) for the states on the FAs marked in red dots [see Fig. 3(a)]. We observe that the FA states are either localized on the top surface ($y = L_y$) or at the bottom surface ($y = 1$). Specifically, the states in the FA$_2$ are localized at the bottom surface [see Fig. 3(b)]. We also note that on FA$_2$ the states away from the WNs, i.e., close to the center of the arc, are distinctly localized at the bottom surface [see curves 2 and 3 in Fig. 3(b)]. On the other hand, the states close to the WNs have significant overlap with the bulk states [see curve 1 in Fig. 3(b)]. This happens since the FAs leak into the bulk states near the WNs as mentioned in the previous section. Similarly, we also choose points from FA$_1$, FA$_3$, FA$_4$ [red colored dots marked by 4, 5, 6 in Fig. 3(a)] and present the behavior of $|\Psi|^2$ in Fig. 3(c). We find that FA$_1$ and FA$_4$ states are localized on the top surface, while those for FA$_2$ and FA$_3$ are localized at the bottom surface. Note that we show curve 2 in panel (b) too for the sake of comparison and clarity.

Here, we explore the spin textures of the FA states. We compute the expectation value of the spin operator along the z direction for each site along the y direction. To perform that, we expand the states in terms of the basis $|y, \alpha, \sigma\rangle$ with $y = 1, 2, \ldots, L_y; \sigma = \uparrow, \downarrow; \alpha = A, B$ for the slab geometry as

$$\left|\psi^{\rm FA}_{k_xk_zy}\right\rangle = \sum_{y=1}^{L_y}\sum_{\sigma=\uparrow,\downarrow}\sum_{\alpha=A,B} d(y,\alpha,\sigma)\,|y,\alpha,\sigma\rangle\,. \tag{8}$$

The spin-polarization along the z direction is defined as

$$S_z = \frac{1}{2}(|\uparrow\rangle\langle\uparrow| - |\downarrow\rangle\langle\downarrow|), \tag{9}$$

and the corresponding expectation value of S_z is given by

$$\left\langle\psi^{\rm FA}_{k_xk_zy}\right| S_z \left|\psi^{\rm FA}_{k_xk_zy}\right\rangle = \sum_{y=1}^{L_y}\sum_{\alpha=A,B}\frac{1}{2}[|d(y,\alpha,\uparrow)|^2 - |d(y,\alpha,\downarrow)|^2]. \tag{10}$$

We show the spin textures, i.e., the expectation values $\langle S_z\rangle$ taking into account the FA states in Fig. 3(a) for the sake of understanding. The up (down) arrows, $\uparrow$ ($\downarrow$), are used to express the positive (negative) values of $\langle S_z\rangle$. The length of each arrow is proportional to the value of $\langle S_z\rangle$ with a maximum value of $1/2$. We observe that the states on FAs exhibit both up and down spin polarization. Specifically, the states on FA$_1$ and FA$_2$ (FA$_3$ and FA$_4$) host down (up) spin polarized states. Now, focusing on FA$_1$ and FA$_4$, we infer that the electrons localized on the top surface have spin polarizations along both positive and negative z axis. Notably, this information is very crucial

for the formation of the superconducting pair between the surface state electrons indicating a strong possibility of Andreev reflection in the WSM-WSC hybrid junction mediated by the surface states. Similarly, the FA_2 and FA_3 states are localized at the bottom surface and contain both spin polarizations. Note that $|\langle S_z\rangle| \neq 1/2$ for all the states on FAs. States in the center of FAs have $|\langle S_z\rangle| = 1/2$ while states close to the WNs are partially spin polarized. The presence of TRS in the system is also reflected in the spin textures of FAs since any FA state with (k_x, k_z) and its time-reversed partner $(-k_x, -k_z)$ have spin polarizations opposite to each other.

C. Nanowire geometry

With the understanding of the surface FA states in WSM slab geometry, we now turn our focus to the NW geometry, which is the prime concern of our present work. The size of the NW along the x and y directions is L_x and L_y, respectively, where $L_x = L_y$. To find the band structure of the NW, we consider the NW to be infinite along the z direction so that the momentum along the z direction becomes well defined (PBC), while the momenta along the x and y directions remain ill defined (OBC) due to the finite size.

1. WSM NW

For the WSM NW, we obtain the Hamiltonian by performing the inverse FT along the x and y directions using

$$c_{\mathbf{k},\alpha,\sigma} = \frac{1}{\sqrt{L_x L_y}} \sum_{x=1}^{L_x} \sum_{y=1}^{L_y} e^{i(k_x x + k_y y)} c_{x\,y\,k_z,\alpha,\sigma},$$

$$\psi_{\mathbf{k}} = \frac{1}{\sqrt{L_x L_y}} \sum_{x=1}^{L_x} \sum_{y=1}^{L_y} e^{i(k_x x + k_y y)} \psi_{x\,y\,k_z,\alpha,\sigma}. \tag{11}$$

With this transformation, the Hamiltonian takes the form

$$\mathcal{H}^{\mathrm{NW}} = \sum_{k_z} \sum_{x,x'=1}^{L_x} \sum_{y,y'=1}^{L_y} \psi^{\dagger}_{x\,y\,k_z} \mathcal{H}^{\mathrm{NW}}_{\mathrm{WSM}}(x, x', y, y', k_z) \psi_{x',y',k_z},$$

where

$$\begin{aligned}\mathcal{H}^{\mathrm{NW}}_{\mathrm{WSM}}(x, x', y, y', k_z) &= \left(\frac{\lambda_x}{2i}\tau_1 s_3 + t\tau_3 s_2\right)\delta_{x,x'+1}\delta_{y,y'} + [\beta\tau_2 s_2 + (m - 4t)\tau_0 s_0 \\ &\quad + \cos k_z \tau_3 s_0]\delta_{x,x'}\delta_{y,y'} \\ &\quad + \left[\frac{\lambda_y}{2i}\tau_2 s_0 + \frac{\alpha}{2i}\tau_1 s_2 + t\tau_3 s_0\right]\delta_{x,x'}\delta_{y,y'+1} + \mathrm{H.c.}, \end{aligned} \tag{12}$$

For the WSM NW, we consider $L_x = L_y = W = 20$ and numerically diagonalize the above Hamiltonian for each value of k_z. We present the eigenspectrum as a function of k_z in Fig. 4(a) employing both PBC and OBC. As mentioned earlier, in OBC we obtain the information about both bulk and surface states of the system while in PBC information about only the bulk states can be achieved.

For TRS-broken WSM NW, it has already been shown in Ref. [57] that the bulk states are gapped out due to the finite-size effect, and within the bulk gap, E_g^{bulk}, only surface states exist. A finite-size gap, E_g^{surface}, is also developed on the surface state spectrum but the bulk confinement gap is larger than that developed on the surface. Specifically, $E_g^{\mathrm{bulk}} \sim 1/W$ whereas $E_g^{\mathrm{surface}} \sim 1/4W$. This feature is also observed in the present model where the bulk gap $E_g = 0.05t$ and $E_g^{\mathrm{bulk}} \sim 1/W$ and within the energy regime, $[-E_g, E_g]$, only surface states are present [shown by teal color in Fig. 4(a)]. This behavior is not present in the slab geometry where both the bulk and surface states are gapless, and thus distinguishing the surface states from the bulk does not seem possible in the WSM slab. Therefore NW geometry is the possible platform where the surface states can be clearly distinguished from the bulk states and can possibly be probed in such a way that the contribution of the bulk states in the measurement can be excluded.

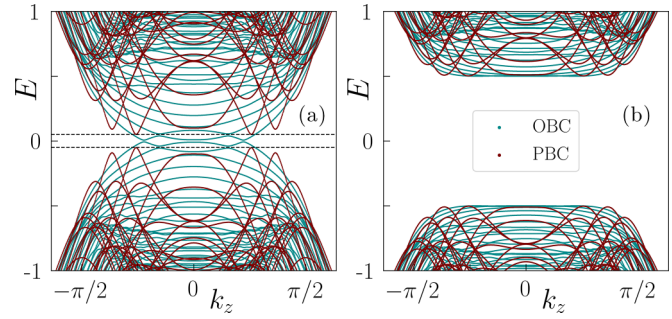

FIG. 4. Band structure is shown as a function of k_z for (a) WSM and (b) WSC NW choosing $L_x = L_y = 20$ and employing both OBC (teal color) and PBC (dark-red color) along x and y directions. The finite-size gap, E_g ($= 0.05t$), in WSM NW bulk band structure is highlighted by the dashed lines.

Furthermore, similar to the slab geometry, we here discuss the properties of FAs in the NW geometry. In the NW geometry, FAs are present within the bulk confinement gap, i.e., $-E_g \leqslant E \leqslant E_g$. From the band structure, presented in Fig. 4(a) (shown by teal color), it is clear that only the lowest energy band with $E>0$ is present inside the confinement gap, E_g, between the WNs ($-k_z^0 \leqslant k_z \leqslant k_z^0$). Therefore, we focus on this band to obtain the properties of FAs. First, we compute $|\Psi_{n,k_z}(x, y)|^2$ as a function of position, (x, y), with $k_z = 0$ where Ψ_{n,k_z} is the eigenstate of the Hamiltonian [Eq. (12)] corresponding to the lowest positive energy band having momentum, k_z. We depict the probability $|\Psi_{n,k_z}(x, y)|^2$ in Fig. 5(a) and establish that the states within the bulk gap, E_g, are indeed localized on the surface of the NW with significant population in the $y = 1$ and $y = L_y$ ($= 20$) surface. Then, we compute the expectation value of polarization along the z axis in the earlier mentioned energy band and show it in Fig. 5(b). We observe that the states within this band carry polarization along both positive and negative z directions. The presence of both up and down spin polarized states on the NW surface is very crucial for generating AR process mediated via FAs in a WSM/WSC NW junction [see Fig. 1(b)], which we discuss extensively in Sec. III B.

2. WSC NW

After explaining the nature of FAs in WSM NW, let us discuss the effect of superconductivity in the NW geometry. We consider an s-wave spin-singlet intraorbital pairing with amplitude Δ in both the bulk and surface of the NW. Since

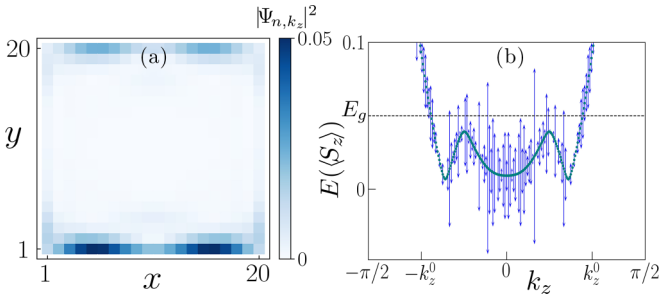

FIG. 5. (a) Probability of wave function $|\Psi_{n,k_z}|^2$ is shown as a function of the position x and y with $k_z = 0$ for the state corresponding to the lowest positive energy band within the gap E_g as illustrated in Fig. 4(a). (b) Average spin polarization $\langle S_z \rangle$ for those states are depicted by the blue arrows on top of the lowest positive energy band (teal color). The direction and length of all arrows carry the same meaning as mentioned in Fig. 3.

the surface states contain electrons with both spin polarizations (as shown in the slab geometry calculations), s-wave spin-singlet pairing between the electrons is expected to be prominent over the spin-triplet pairing. Similar to the WSM NW, we perform the inverse FT to obtain the WSC NW Hamiltonian as

$$\begin{aligned}\mathcal{H}^{\rm NW}_{\rm WSC}(x,x',y,y',k_z) &= \left(\frac{\lambda_x}{2i}\tau_1 s_3 \pi_0 + t\,\tau_3 s_2 \pi_3\right)\delta_{x,x'+1}\delta_{y,y'} \\ &+ [\beta \tau_2 s_2 \pi_3 + (m-4t)\tau_0 s_0 \pi_3 + \cos k_z \tau_3 s_0 \pi_3]\delta_{x,x'}\delta_{y,y'} \\ &+ \left[\frac{\lambda_y}{2i}\tau_2 s_0 + \frac{\alpha}{2i}\tau_1 s_2 \pi_3 + t\,\tau_3 s_0\right]\delta_{x,x'}\delta_{y,y'+1} \\ &+ \Delta \delta_{x,x'}\delta_{y,y'}\tau_0 s_2 \pi_2 + \text{H.c.} \end{aligned} \tag{13}$$

We then numerically diagonalize the Hamiltonian considering the same system size as mentioned for the WSM NW and plot the band structure as a function of k_z in Fig. 4(b) employing both OBC and PBC. We observe that due to the superconducting correlation, both bulk and surface states acquire a gap of magnitude Δ.

III. CONDUCTANCE

In this section, we present our numerical results for the conductance in the WSM and WSM/WSC NW setups.

A. WSM NW

Let us begin by analyzing the transport signatures of FAs in an ISB WSM NW based two-terminal setup. For this purpose, we first exclude the WSC NW part in Fig. 1(b) by extending the WSM NW and attach two semi-infinite leads at $z = -L/2$ and $z = L/2$. We model both the leads using the same Hamiltonian which is used to describe the WSM NW. The chemical potential at the left (right) lead is fixed at $\mu_{\rm L}$ ($\mu_{\rm R}$). Under the application of voltage bias, eV ($= \mu_{\rm L} - \mu_{\rm R}$), we compute two-terminal charge transport employing the Landauer formula [82]. To obtain the current traversing through the NW, we first construct the scattering matrix, which relates the incoming propagating modes to the outgoing modes in the leads with the central WSM NW being considered as the scatterer. Incoming and outgoing states and the scattering matrix are defined as

$$\Psi^{\rm in} = \left[\psi_1^{\rm L}, \psi_2^{\rm L}, \ldots, \psi_{4N_{\rm L}}^{\rm L}, \psi_1^{\rm R}, \psi_2^{\rm R}, \ldots, \psi_{4N_{\rm R}}^{\rm R}\right]^T, \tag{14}$$

$$\Phi^{\rm out} = \left[\phi_1^{\rm L}, \phi_2^{\rm L}, \ldots, \phi_{4N_{\rm L}}^{\rm L}, \phi_1^{\rm R}, \phi_2^{\rm R}, \ldots, \phi_{4N_{\rm R}}^{\rm R}\right]^T,$$

$$\Phi^{\rm out} = \hat{S}\Psi^{\rm in}, \tag{15}$$

where $\psi_i^{\rm L(R)}$ is the incoming state from the left (right) lead in the ith mode. Here, $4N_{\rm L}$ ($4N_{\rm R}$) is the number of occupied modes/channels in the left (right) lead for a given voltage bias eV (including both spin and orbital degrees of freedom). Similarly, $\phi_i^{\rm L(R)}$ is the outgoing state into the left (right) lead in the ith mode after the scattering event takes place. Here, T denotes the transpose operation. The unitary scattering matrix $\hat{S}$ of dimension $(4N_{\rm L} + 4N_{\rm R}) \times (4N_{\rm L} + 4N_{\rm R})$ reads

$$\hat{S} = \begin{bmatrix} \hat{r} & \hat{t'} \\ \hat{t} & \hat{r'} \end{bmatrix}, \tag{16}$$

where, $\hat{r}$ ($\hat{r'}$) is a square matrix of dimension $4N_{\rm L} \times 4N_{\rm L}$ ($4N_{\rm R} \times 4N_{\rm R}$) and $\hat{t}$ ($\hat{t'}$) is a matrix of dimension $4N_{\rm R} \times 4N_{\rm L}$ ($4N_{\rm L} \times 4N_{\rm R}$). Physically, $\hat{r}$ ($\hat{r'}$) represents the reflection matrix with elements $r_{i,j}$ ($r'_{i,j}$) being the amplitude of reflection from the jth mode to the ith mode in the left (right) lead. Similarly, $\hat{t}$ ($\hat{t'}$) represents the transmission matrix with elements $t_{i,j}$ ($t'_{i,j}$) denoting the amplitude of the transmission from the jth mode in the left (right) lead to the ith mode in the right (left) lead following the unitarity condition: $r^\dagger r + t^\dagger t = \mathcal{I}$. Within this formalism, the two-terminal conductance at zero temperature can be obtained using the Landauer formula given by [82]

$$G_{\rm N}(eV) = G_0\, {\rm Tr}[t^\dagger t]|_{E=eV}, \tag{17}$$

where $G_0 = e^2/h$ is the unit of quantum conductance. The scattering amplitudes can be calculated numerically using the Python package KWANT [83].

We depict the two-terminal conductance in the WSM NW setup in units of quantum conductance as a function of voltage bias, eV, in Fig. 6(a) assuming the length along the z direction is $L_z = 80$ lattice sites. We observe that conductance initially increases in steps of G_0 and a plateau-like behavior appears after that. For a more clear understanding we refer to the inset of Fig. 6(a). However, when we increase the bias voltage, the steplike behavior is lost and a continuous enhancement in conductance is observed. Similar behavior of the conductance has also been observed for TRS-broken WSM NW [57]. Interestingly, in the case of ISB WSM NW, the quantization of the conductance occurs in steps of $2G_0$, whereas in the case of TRS-broken WSM NW, the steps appear in units of G_0 as shown in Ref. [57]. This happens due to the presence of four FAs (two on each surface) in such system as compared to TRS-broken WSM where two FAs are present. The steplike behavior appears due to the FA surface states within the finite size gap in the system, while the following continuous enhancement happens since the bulk states start contributing. Due to the semimetallic nature of the bulk spectrum, the conductance for the higher bias voltages varies as $(eV)^2$.

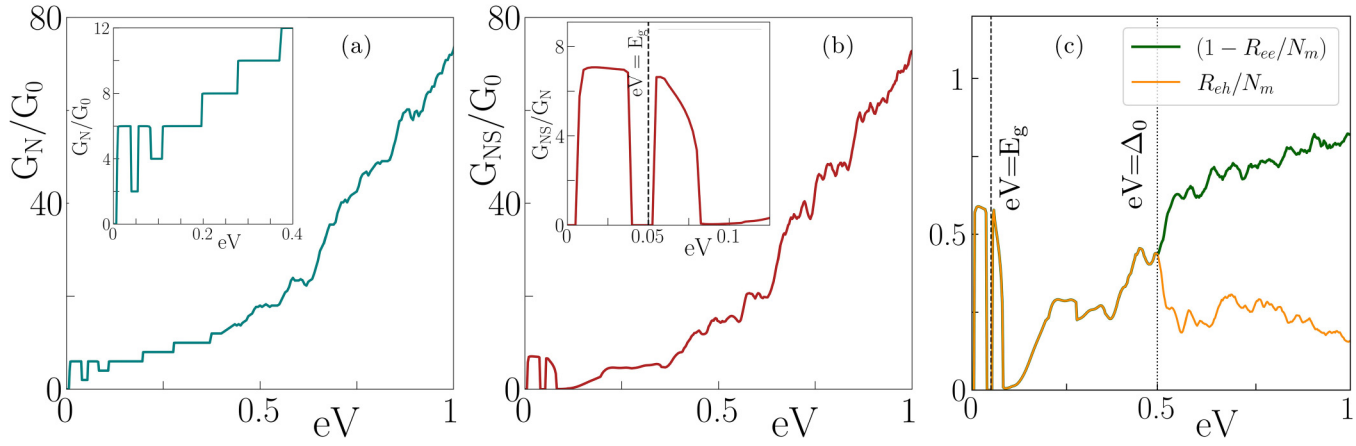

FIG. 6. Two-terminal conductance in units of quantum conductance, $G_0 = (e^2/h)$, is illustrated as a function of voltage bias eV in (a) WSM NW and (b), (c) WSM/WSC NW hybrid junction considering $L_x = L_y = 20$ and $L_z = 80$ lattice sites. (c) $(1 - R_{ee}/N_m)$ and R_{eh}/N_m are depicted as a function of voltage bias eV, explicitly exhibiting the contribution to conductance via AR process within the bulk confinement gap ($eV < E_g$) and superconducting gap ($eV < \Delta_0$).

In clean systems, the conductance does not depend on the length of the WSM NW along the z direction because of phase-coherent transport along the NW axis considering the same Hamiltonian for the leads. Increasing the system size along the transverse directions does not affect the qualitative picture of the conductance plot, but the quantitative behavior of the conductance changes since both E_g^{bulk} ($\sim 1/W$) and E_g^{surface} ($\sim 1/4W$) decrease. Additionally, increasing the value of L_x and L_y usually enhances the number of transverse modes in the lead spectrum. Hence, the occupancy of propagating modes increases within the leads for a given voltage bias, which in turn can enhance the conductance according to Eq. (17).

B. WSM/WSC NW

Here, we discuss another main finding of our analysis which deals with the transport signatures of the FAs in the WSM/WSC NW hybrid junction. For this purpose, we consider the geometry shown in Fig. 1(b) under the application of voltage bias eV. We model this hybrid setup using the Hamiltonian in Eq. (13). The uniform superconducting pairing potential is chosen as

$$\Delta(x, y, z) = \begin{cases} \Delta_0 & \forall z > 0,\ x, y \in (0, W), \\ 0 & \forall z < 0,\ x, y \in (0, W). \end{cases} \tag{18}$$

The leads are also modeled by the same Hamiltonian as mentioned in Eq. (13). The left lead is chosen to be non-superconducting ($\Delta_0 = 0$), while the right lead possesses a superconducting pairing gap as mentioned above. This hybrid setup mimics a normal-superconductor (NS) junction.

The additional mechanism that comes into play while considering charge transport in such superconducting hybrid junction is the Andreev reflection (AR) where an incoming right-moving electron from the left lead with spin σ combines with another electron with opposite spin $\bar{\sigma}$ to form a spin-singlet Cooper pair leaving behind a hole that reflects back from the interface. The Cooper pairs, formed at the interface, propagate through the WSC and give rise to a supercurrent [84]. In our work, the primary motivation to capture the signatures of FAs via the AR lies in these spin textures of the FAs [see Figs. 3(a)–3(c)]. Note that within a particular surface, the spin polarization of electrons along the z direction has components along both positive and negative z axes, indicating the strong possibility of AR mediated via the FAs.

To find the conductance in this hybrid junction, we employ the scattering matrix formalism which now takes more complex form compared to the bare WSM NW due to the presence of the AR process. It can now be written as

$$\begin{bmatrix} \Phi_e^{\text{L}} \\ \Phi_h^{\text{L}} \\ \Phi_e^{\text{R}} \\ \Phi_h^{\text{R}} \end{bmatrix} = \mathcal{S}_{\text{NS}} \begin{bmatrix} \Psi_e^{\text{L}} \\ \Psi_h^{\text{L}} \\ \Psi_e^{\text{R}} \\ \Psi_h^{\text{R}} \end{bmatrix}, \tag{19}$$

where, $\Psi_{e(h)}^{\text{L(R)}}$ is a column matrix of dimension $4N_{\text{L(R)}}$ and it represents the incoming electron (hole) from the left (right) lead. Similarly, $\Phi_{e(h)}^{\text{L(R)}}$ designates the outgoing electron (hole) in the left (right) lead. The scattering matrix $\mathcal{S}_{\text{NS}}$ can be written as

$$\mathcal{S}_{\text{NS}} = \begin{bmatrix} r_{ee} & r_{eh} & t'_{ee} & t'_{eh} \\ r_{he} & r_{hh} & t'_{he} & t'_{hh} \\ t_{ee} & t_{eh} & r'_{ee} & r'_{eh} \\ t_{he} & t_{hh} & r'_{he} & r'_{hh} \end{bmatrix}, \tag{20}$$

where r_{ee}, r_{eh}, r_{he}, and r_{hh} denote the complex matrices with dimension $4N_{\text{L}} \times 4N_{\text{L}}$. The matrix element $(r_{\alpha\beta})_{ij}$ represents the amplitude of reflection from the particle type β in the jth channel of the left lead to the particle type α in the ith channel of left lead with $\alpha, \beta = (e, h)$. For our purpose, it is now sufficient to focus on the reflection matrices in the left lead, i.e.,

$$\mathcal{R}_{\text{NS}} = \begin{bmatrix} r_{ee} & r_{eh} \\ r_{he} & r_{hh} \end{bmatrix}. \tag{21}$$

The reason behind writing Eq. (21) is the absence of the quasiparticle states within the superconducting gap which prevents the transmission of electron-like (or hole-like) particles from

the left normal lead to the right superconducting lead. Similarly, there are no single-particle states present inside the right lead to propagate through the WSC and reach the left lead. In this circumstance, within the subgap regime, the only possible scattering processes are reflection of electrons as an electron (normal reflection), denoted by the r_{ee} matrix in Eq. (21), and AR. Note that it follows the unitarity relation of $\mathcal{R}_{\rm NS}$ as given by

$$r_{ee}^{\dagger} r_{ee} + r_{he}^{\dagger} r_{he} = \mathcal{I}. \tag{22}$$

With this understanding, we now employ the Blonder-Tinkham-Klapwijk (BTK) formalism to obtain the conductance of this hybrid junction as [84–87]

$$G_{\rm NS}(eV) = G_0[N_m(E) - R_{ee}(E) + R_{eh}(E)]|_{E=eV}, \tag{23}$$

where $R_{ee}(E) = \mathrm{Tr}(r_{ee}^{\dagger} r_{ee})$ and $R_{eh}(E) = \mathrm{Tr}(r_{he}^{\dagger} r_{he})$. $N_m(eV)$ is the number of occupied modes/channels in the left lead for a given voltage bias eV. Using the Python package KWANT [83], we obtain the reflection matrices, r_{ee} , r_{eh}, and also N_m to compute the conductance.

We depict the conductance, $G_{\rm NS}$, as a function of voltage bias, eV, in Fig. 6(b). We also show $(N_m - R_{ee})$ and R_{eh} for comparison, normalized by the number of available modes in the left lead (N_m), as a function of eV in Fig. 6(c). For the bias voltage less than the bulk confinement gap ($eV < E_g$) where only the FA surface states exist [see Fig. 4(a)], we find $G_{\rm NS}$ exhibits nonzero value and becomes almost equal to $7G_0$ [see Fig. 6(b)]. This is concomitant with nonzero value of R_{eh} [see Fig. 6(c)] which establishes the possibility of AR mediated by FAs which is one of the main claims of the present work: capturing the signatures of FAs in this superconducting hybrid junction. In the subgapped regime ($eV < \Delta_0$), $(N_m - R_{ee})/N_m$ and R_{eh}/N_m identically follow each other which can be explained using the unitarity relation of $\mathcal{R}_{\rm NS}$ [see Eq. (22)] as $R_{eh} = \mathrm{Tr}(r_{he}^{\dagger} r_{he}) = \mathrm{Tr}(\mathcal{I} - r_{ee}^{\dagger} r_{ee}) = N_m - R_{ee}$. For $eV > E_g$, we observe $G_{\rm NS}$ suddenly drops to zero and then gradually increases with the voltage bias as shown in Fig. 6(b). For better clarity, we also refer to the inset of Fig. 6(b). When $eV > \Delta_0$, $R_{eh} \neq (N_m - R_{ee})$ and R_{eh} decays with the increase in voltage bias. This is due to the presence of finite quasiparticle density of states for $eV > \Delta_0$, which allows t_{ee} and t_{he} matrices to be nonzero, and as a result, Eq. (22) does not hold.

Interestingly, in the subgapped regime, $G_{\rm NS}/G_0$ is not quantized in the regime where $G_{\rm N}/G_0$ exhibits quantized values as shown in the inset of Fig. 6(a). This is unusual since in the absence of any interfacial insulating barrier (transparent limit), the subgap conductance is expected to be twice the conductance in the absence of the superconductors, i.e., $G_{\rm NS} = 2G_{\rm N}$ (see Ref. [84] for details). This peculiarity can originate from two correlated reasons as follows. First, even though FAs host both up and down spin textures, the expectation value of spin polarization $|\langle S_z \rangle| \neq 1/2$, for all states on the FAs. This makes the AR deviated from the unit probability within the subgap regime even in the transparent limit which indicates that all the electrons may not reflect as holes from the interface. Thus, perfect AR does not take place restricting the quantization of $G_{\rm NS}$. Second, in Fig. 6(c), we note the finite value of R_{ee}/N_m (since N_m is quantized in the region of concern) even in the absence of any insulating barrier at the interface. Such normal reflection probability can originate from the interchannel scatterings in the WSM NW which can also prohibit the perfect quantization.

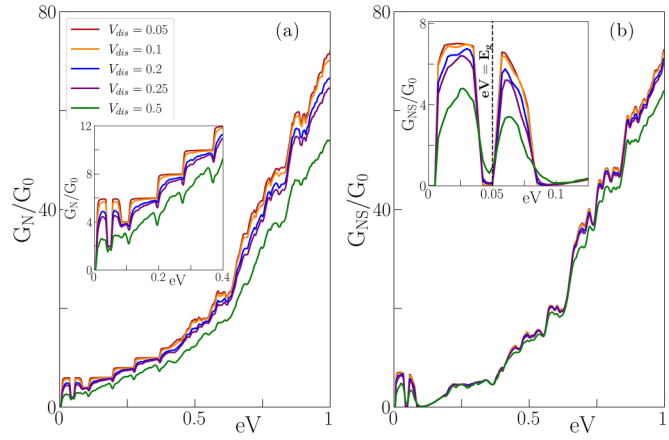

FIG. 7. Two-terminal conductance is demonstrated for a disordered (a) WSM NW and (b) WSM/WSC NW junction as a function of voltage bias, eV, choosing various disorder strengths, $V_{\rm dis}$. Dimensions of the NWs are considered to be the same as mentioned in Fig. 6. We choose the delta-correlated disorder to be uniformly distributed between $[-V_{\rm dis}/2, V_{\rm dis}/2]$. We consider 30 disorder configurations for our analysis.

IV. STABILITY AGAINST DISORDER

So far, all the results are presented for clean systems. We now extend our analysis to include the effect of disorder and investigate the robustness of our results in both the WSM NW and WSM/WSC NW junction. Usually, the bulk properties of WSM are robust against disorder unless the disorder strength is strong enough to allow internode scatterings and create a gap to destroy the topological phase [35–37,39]. Specifically, to check the stability of FAs against the disorder that breaks translational symmetry of the system, we consider random quenched disorder which is delta-correlated, in terms of an on-site energy potential in the Hamiltonian, as

$$\mathcal{H}_{\rm dis}(\mathbf{r}) = V(r)\Gamma, \tag{24}$$

where $V(r)$ is random number uniformly distributed in the range $[-V_{\rm dis}/2, V_{\rm dis}/2]$ and $V_{\rm dis}$ is referred to as the disorder strength. We choose $\Gamma = \tau_0 s_0$ for WSM NW and $\Gamma = \tau_0 s_0 \pi_3$ for WSM/WSC NW junction. For the hybrid junction, the disorder is considered only in the $-L/2 < z < 0$ region [88–90].

To compute the conductance, $G_{\rm N}$ and $G_{\rm NS}$ [Eq. (17) and Eq. (23)], in the presence of disorder, we again employ scattering matrix formalism and extract the reflection (r_{ee}, r_{he}) and transmission (t) matrices using KWANT [83]. We show the disorder-averaged conductance, G_N and $G_{\rm NS}$, as a function of voltage bias for various disorder strengths in Figs. 7(a) and 7(b), respectively. The results are obtained after averaging over 30 disorder configurations.

The average energy level spacing of the FAs in the WSM NW geometry is estimated approximately as $\Delta E_l = 0.08t$ where the average level broadening induced by disorder is $\Delta E_{\rm dis} = \frac{\pi}{3} V_{\rm dis}^2$ [57]. From here, we can estimate the critical disorder strength above which the quantized conductance plateau does not survive as $V_{\rm dis}^{\rm c} = \sqrt{3\Delta E_l/\pi} = 0.27$. From

Fig. 7(a) and Fig. 7(b), we can verify that the quantized conductance plateau, arising due to the FA surface states, survive up to the disorder strength, $V_{\rm dis} = 0.25$ [see the inset of Fig. 7(a) for better clarity], above which the conductance quantization is diminished. Similarly, in the case of the WSM/WSC NW junction, we observe our results to be sustained up to sufficiently large disorder strength. Note that, unlike the clean system, where the conductance is independent of NW length, in the presence of disorder, conductance depends on the NW length since phase coherency is lost. In particular, keeping the disorder strength moderate, the conductance decreases as the NW length is increased.

V. SUMMARY AND CONCLUSIONS

To summarize, in this article, we have explored an ISB WSM with four bulk Weyl nodes in the k_x-k_z plane. We have analyzed the properties of FAs in a slab geometry considering the y direction to be finite and found both up and down spin polarized FA states at both $y = 1$ and $y = L_y$ surfaces. We have then investigated the FAs with further confinement in another direction which leads to a NW geometry. In the WSM NW setup, due to the finite-size effects, both the bulk and surface states are gapped out. Interestingly, the surface state gap is still smaller than the bulk confinement gap, thus allowing one to probe only surface states and explore various transport signatures mediated due to only FAs. We also analyze the localization properties of FAs in the NW geometry and find the spin textures similar to that in WSM slab. To obtain the conductance, we have extracted the matrix elements within the scattering matrix formalism using the Python package KWANT [83]. Specifically, we have computed the two-terminal conductance of the WSM NW using the Landauer formula and observed the conductance quantization in units of $2e^2/h$. To capture the signatures of FAs in AR, we have constructed a WSM/WSC NW hybrid junction and found the conductance using the BTK formula [84–87]. We show that the signatures of the FAs can be separated out via the AR process too. Note that the conductance in this hybrid setup is not quantized. Finally, we have investigated the stability of the conductance against the random on-site disorder potential in both the WSM NW and WSM/WSC NW hybrid junction and find our results to be robust against disorder strength up to a critical value $V_{\rm dis}^{\rm c}$.

Here we convey a few comments as far as the experimental feasibility of our transport setups is concerned. Earlier theoretical works to capture the signature of FAs are mainly based on TRS-broken WSM [56,57,75,91]. In reality, TRS-broken WSM needs application of large magnetic field [92], whereas experimentally observed WSM phases are mostly ISB, e.g., TaAs, TaP, NbAs, NbP, etc. [19–34]. Specifically, there exist several works on the Dirac semimetal Cd_3As_2 NW where WSM phase can be achieved by applying a strong external magnetic field (∼1 T) with diameter of the NW ∼20–100 nm [49,51,93,94]. Application of large external magnetic field can generate Landau levels and the phenomenon of chiral anomaly may affect the results. Hence, our work based on ISB WSM NW is out of such scope and carries potential from the practical point of view. Note that the bulk gap in NW due to quantum confinement is observed to be ∼10 meV with gap size being $\sim\hbar v_f\sqrt{\pi/S}$ (v_f, S being the Fermi velocity and cross section of the NW, respectively). For a typical value of $v_f \sim 10^5$ m/s in Cd_3As_2 NW and $W \sim 20$ Å (for lattice constant ∼1 Å), gap size comes out to be ∼100 meV which closely resembles the bulk confinement gap, $E_g^{\rm bulk} = 0.05t \sim 50$ meV (assuming $t \sim$ eV), obtained in our numerical calculation of band structure. Therefore, the realization of our theoretical results regarding FA mediated transport is subjected to the chemical potential lying within the bulk confinement gap, i.e., $\mu \lesssim$ 50–100 meV. Finally, the realization of a WSC can be achieved by introducing a common s-wave superconductor such as Al or Nb in close proximity to the WSM NW [95]. Thus, our proposal serves as a possible potential experimental test bed, offering experimentalists the opportunity and challenge to validate our findings.

ACKNOWLEDGMENTS

A.P. acknowledges A. Kundu, S. Das, A. K. Ghosh, and P. Chatterjee for stimulating discussions. A.P. and A.S. acknowledge SAMKHYA: High-Performance Computing Facility provided by Institute of Physics, Bhubaneswar, for numerical computations. P.D. acknowledges Department of Space, Government of India, for all support at Physical Research Laboratory (PRL) and Department of Science and Technology (DST), Government of India (through SERB Start-up Research Grant, File No. SRG/2022/001121) for the financial support.

[1] N. P. Armitage, E. J. Mele, and A. Vishwanath, Weyl and Dirac semimetals in three-dimensional solids, Rev. Mod. Phys. **90**, 015001 (2018).
[2] S. Rao, Weyl semimetals: A short review, J. Indian Inst. Sci. **96**, 145 (2016).
[3] T. M. McCormick, I. Kimchi, and N. Trivedi, Minimal models for topological Weyl semimetals, Phys. Rev. B **95**, 075133 (2017).
[4] B. Yan and C. Felser, Topological materials: Weyl semimetals, Annu. Rev. Condens. Matter Phys. **8**, 337 (2017).
[5] A. Burkov, Weyl metals, Annu. Rev. Condens. Matter Phys. **9**, 359 (2018).
[6] P. A. M. Dirac and R. H. Fowler, The quantum theory of the electron, Proc. R. Soc. London Ser. A **117**, 610 (1928).
[7] H. Weyl, Elektron und gravitation. I, Z. Phys. **56**, 330 (1929).
[8] S. Murakami, Phase transition between the quantum spin Hall and insulator phases in 3D: Emergence of a topological gapless phase, New J. Phys. **9**, 356 (2007).
[9] M. M. Vazifeh and M. Franz, Electromagnetic response of Weyl semimetals, Phys. Rev. Lett. **111**, 027201 (2013).
[10] A. A. Burkov and L. Balents, Weyl semimetal in a topological insulator multilayer, Phys. Rev. Lett. **107**, 127205 (2011).
[11] A. A. Burkov, M. D. Hook, and L. Balents, Topological nodal semimetals, Phys. Rev. B **84**, 235126 (2011).

[12] A. A. Zyuzin, S. Wu, and A. A. Burkov, Weyl semimetal with broken time reversal and inversion symmetries, Phys. Rev. B **85**, 165110 (2012).

[13] A. A. Zyuzin and A. A. Burkov, Topological response in Weyl semimetals and the chiral anomaly, Phys. Rev. B **86**, 115133 (2012).

[14] G. B. Halász and L. Balents, Time-reversal invariant realization of the Weyl semimetal phase, Phys. Rev. B **85**, 035103 (2012).

[15] C.-X. Liu, P. Ye, and X.-L. Qi, Chiral gauge field and axial anomaly in a Weyl semimetal, Phys. Rev. B **87**, 235306 (2013).

[16] X. Wan, A. M. Turner, A. Vishwanath, and S. Y. Savrasov, Topological semimetal and Fermi-arc surface states in the electronic structure of pyrochlore iridates, Phys. Rev. B **83**, 205101 (2011).

[17] T. Bzdušek, A. Rüegg, and M. Sigrist, Weyl semimetal from spontaneous inversion symmetry breaking in pyrochlore oxides, Phys. Rev. B **91**, 165105 (2015).

[18] W. Witczak-Krempa and Y. B. Kim, Topological and magnetic phases of interacting electrons in the pyrochlore iridates, Phys. Rev. B **85**, 045124 (2012).

[19] B. Q. Lv, N. Xu, H. M. Weng, J. Z. Ma, P. Richard, X. C. Huang, L. X. Zhao, G. F. Chen, C. E. Matt, F. Bisti, V. N. Strocov, J. Mesot, Z. Fang, X. Dai, T. Qian, M. Shi, and H. Ding, Observation of Weyl nodes in TaAs, Nat. Phys. **11**, 724 (2015).

[20] B. Q. Lv, H. M. Weng, B. B. Fu, X. P. Wang, H. Miao, J. Ma, P. Richard, X. C. Huang, L. X. Zhao, G. F. Chen, Z. Fang, X. Dai, T. Qian, and H. Ding, Experimental discovery of Weyl semimetal TaAs, Phys. Rev. X **5**, 031013 (2015).

[21] B. Q. Lv, S. Muff, T. Qian, Z. D. Song, S. M. Nie, N. Xu, P. Richard, C. E. Matt, N. C. Plumb, L. X. Zhao, G. F. Chen, Z. Fang, X. Dai, J. H. Dil, J. Mesot, M. Shi, H. M. Weng, and H. Ding, Observation of Fermi-arc spin texture in TaAs, Phys. Rev. Lett. **115**, 217601 (2015).

[22] L. Lu, Z. Wang, D. Ye, L. Ran, L. Fu, J. D. Joannopoulos, and M. Soljačić, Experimental observation of Weyl points, Science **349**, 622 (2015).

[23] S.-Y. Xu, I. Belopolski, D. S. Sanchez, C. Zhang, G. Chang, C. Guo, G. Bian, Z. Yuan, H. Lu, T.-R. Chang, P. P. Shibayev, M. L. Prokopovych, N. Alidoust, H. Zheng, C.-C. Lee, S.-M. Huang, R. Sankar, F. Chou, C.-H. Hsu, H.-T. Jeng, A. Bansil, T. Neupert, V. N. Strocov, H. Lin, S. Jia, and M. Z. Hasan, Experimental discovery of a topological Weyl semimetal state in TaP, Sci. Adv. **1**, e1501092 (2015).

[24] S.-Y. Xu, N. Alidoust, I. Belopolski, Z. Yuan, G. Bian, T.-R. Chang, H. Zheng, V. N. Strocov, D. S. Sanchez, G. Chang, C. Zhang, D. Mou, Y. Wu, L. Huang, C.-C. Lee, S.-M. Huang, B. Wang, A. Bansil, H.-T. Jeng, T. Neupert, A. Kaminski, H. Lin, S. Jia, and M. Z. Hasan, Discovery of a Weyl fermion state with Fermi arcs in niobium arsenide, Nat. Phys. **11**, 748 (2015).

[25] S.-Y. Xu, I. Belopolski, N. Alidoust, M. Neupane, G. Bian, C. Zhang, R. Sankar, G. Chang, Z. Yuan, C.-C. Lee, S.-M. Huang, H. Zheng, J. Ma, D. S. Sanchez, B. Wang, A. Bansil, F. Chou, P. P. Shibayev, H. Lin, S. Jia, and M. Z. Hasan, Discovery of a Weyl fermion semimetal and topological Fermi arcs, Science **349**, 613 (2015).

[26] A. A. Soluyanov, D. Gresch, Z. Wang, Q. Wu, M. Troyer, X. Dai, and B. A. Bernevig, Type-II Weyl semimetals, Nature (London) **527**, 495 (2015).

[27] P. J. W. Moll, N. L. Nair, T. Helm, A. C. Potter, I. Kimchi, A. Vishwanath, and J. G. Analytis, Transport evidence for Fermi-arc-mediated chirality transfer in the Dirac semimetal Cd_3As_2, Nature (London) **535**, 266 (2016).

[28] Z. Wang, M. G. Vergniory, S. Kushwaha, M. Hirschberger, E. V. Chulkov, A. Ernst, N. P. Ong, R. J. Cava, and B. A. Bernevig, Time-reversal-breaking Weyl fermions in magnetic Heusler alloys, Phys. Rev. Lett. **117**, 236401 (2016).

[29] D.-F. Xu, Y.-P. Du, Z. Wang, Y.-P. Li, X.-H. Niu, Q. Yao, D. Pavel, Z.-A. Xu, X.-G. Wan, and D.-L. Feng, Observation of Fermi arcs in non-centrosymmetric Weyl semi-metal candidate NbP, Chin. Phys. Lett. **32**, 107101 (2015).

[30] T. Ojanen, Helical Fermi arcs and surface states in time-reversal invariant Weyl semimetals, Phys. Rev. B **87**, 245112 (2013).

[31] Y. Sun, S.-C. Wu, and B. Yan, Topological surface states and Fermi arcs of the noncentrosymmetric Weyl semimetals TaAs, TaP, NbAs, and NbP, Phys. Rev. B **92**, 115428 (2015).

[32] B. Feng, Y.-H. Chan, Y. Feng, R.-Y. Liu, M.-Y. Chou, K. Kuroda, K. Yaji, A. Harasawa, P. Moras, A. Barinov, W. Malaeb, C. Bareille, T. Kondo, S. Shin, F. Komori, T.-C. Chiang, Y. Shi, and I. Matsuda, Spin texture in type-II Weyl semimetal WTe_2, Phys. Rev. B **94**, 195134 (2016).

[33] S.-Y. Xu, I. Belopolski, D. S. Sanchez, M. Neupane, G. Chang, K. Yaji, Z. Yuan, C. Zhang, K. Kuroda, G. Bian, C. Guo, H. Lu, T.-R. Chang, N. Alidoust, H. Zheng, C.-C. Lee, S.-M. Huang, C.-H. Hsu, H.-T. Jeng, A. Bansil, T. Neupert, F. Komori, T. Kondo, S. Shin, H. Lin, S. Jia, and M. Z. Hasan, Spin polarization and texture of the Fermi arcs in the Weyl fermion semimetal TaAs, Phys. Rev. Lett. **116**, 096801 (2016).

[34] A. C. Potter, I. Kimchi, and A. Vishwanath, Quantum oscillations from surface Fermi arcs in Weyl and Dirac semimetals, Nat. Commun. **5**, 5161 (2014).

[35] A. Altland and D. Bagrets, Theory of the strongly disordered Weyl semimetal, Phys. Rev. B **93**, 075113 (2016).

[36] H. Shapourian and T. L. Hughes, Phase diagrams of disordered Weyl semimetals, Phys. Rev. B **93**, 075108 (2016).

[37] J. Klier, I. V. Gornyi, and A. D. Mirlin, From weak to strong disorder in Weyl semimetals: Self-consistent Born approximation, Phys. Rev. B **100**, 125160 (2019).

[38] B. Sbierski, G. Pohl, E. J. Bergholtz, and P. W. Brouwer, Quantum transport of disordered Weyl semimetals at the nodal point, Phys. Rev. Lett. **113**, 026602 (2014).

[39] C.-Z. Chen, J. Song, H. Jiang, Q.-F. Sun, Z. Wang, and X. C. Xie, Disorder and metal-insulator transitions in Weyl semimetals, Phys. Rev. Lett. **115**, 246603 (2015).

[40] J. Maciejko and R. Nandkishore, Weyl semimetals with short-range interactions, Phys. Rev. B **90**, 035126 (2014).

[41] W. Witczak-Krempa, M. Knap, and D. Abanin, Interacting Weyl semimetals: Characterization via the topological Hamiltonian and its breakdown, Phys. Rev. Lett. **113**, 136402 (2014).

[42] M. V. Hosseini and M. Askari, Ruderman-Kittel-Kasuya-Yosida interaction in Weyl semimetals, Phys. Rev. B **92**, 224435 (2015).

[43] V. P. J. Jacobs, P. Betzios, U. Gürsoy, and H. T. C. Stoof, Electromagnetic response of interacting Weyl semimetals, Phys. Rev. B **93**, 195104 (2016).

[44] M. Laubach, C. Platt, R. Thomale, T. Neupert, and S. Rachel, Density wave instabilities and surface state evolution in interacting Weyl semimetals, Phys. Rev. B **94**, 241102(R) (2016).

[45] B. Roy, P. Goswami, and V. Juričić, Interacting Weyl fermions: Phases, phase transitions, and global phase diagram, Phys. Rev. B **95**, 201102(R) (2017).

[46] I. Boettcher, Interplay of topology and electron-electron interactions in Rarita-Schwinger-Weyl semimetals, Phys. Rev. Lett. **124**, 127602 (2020).

[47] G. Xu, H. Weng, Z. Wang, X. Dai, and Z. Fang, Chern semimetal and the quantized anomalous Hall effect in $HgCr_2Se_4$, Phys. Rev. Lett. **107**, 186806 (2011).

[48] Y. Sun, S.-C. Wu, M. N. Ali, C. Felser, and B. Yan, Prediction of Weyl semimetal in orthorhombic $MoTe_2$, Phys. Rev. B **92**, 161107(R) (2015).

[49] S. Wang, B.-C. Lin, W.-Z. Zheng, D. Yu, and Z.-M. Liao, Fano interference between bulk and surface states of a Dirac semimetal Cd_3As_2 nanowire, Phys. Rev. Lett. **120**, 257701 (2018).

[50] G. Chen, W. Chen, and O. Zilberberg, Field-effect transistor based on surface negative refraction in Weyl nanowire, APL Mater. **8**, 011102 (2020).

[51] C.-Z. Li, L.-X. Wang, H. Liu, J. Wang, Z.-M. Liao, and D.-P. Yu, Giant negative magnetoresistance induced by the chiral anomaly in individual Cd_3As_2 nanowires, Nat. Commun. **6**, 10137 (2015).

[52] P. Baireuther, J. A. Hutasoit, J. Tworzydło, and C. W. J. Beenakker, Scattering theory of the chiral magnetic effect in a Weyl semimetal: Interplay of bulk Weyl cones and surface Fermi arcs, New J. Phys. **18**, 045009 (2016).

[53] E. V. Gorbar, V. A. Miransky, I. A. Shovkovy, and P. O. Sukhachov, Origin of dissipative Fermi arc transport in Weyl semimetals, Phys. Rev. B **93**, 235127 (2016).

[54] A. Igarashi and M. Koshino, Magnetotransport in Weyl semimetal nanowires, Phys. Rev. B **95**, 195306 (2017).

[55] M. Breitkreiz and P. W. Brouwer, Large contribution of Fermi arcs to the conductivity of topological metals, Phys. Rev. Lett. **123**, 066804 (2019).

[56] D. K. Mukherjee, S. Rao, and S. Das, Fabry-Perot interferometry in Weyl semi-metals, J. Phys.: Condens. Matter **31**, 045302 (2019).

[57] V. Kaladzhyan and J. H. Bardarson, Quantized Fermi arc mediated transport in Weyl semimetal nanowires, Phys. Rev. B **100**, 085424 (2019).

[58] T. Meng and L. Balents, Weyl superconductors, Phys. Rev. B **86**, 054504 (2012).

[59] G. Y. Cho, J. H. Bardarson, Y.-M. Lu, and J. E. Moore, Superconductivity of doped Weyl semimetals: Finite-momentum pairing and electronic analog of the ^{3}He-*A* phase, Phys. Rev. B **86**, 214514 (2012).

[60] S. Uchida, T. Habe, and Y. Asano, Andreev reflection in Weyl semimetals, J. Phys. Soc. Jpn. **83**, 064711 (2014).

[61] U. Khanna, D. K. Mukherjee, A. Kundu, and S. Rao, Chiral nodes and oscillations in the Josephson current in Weyl semimetals, Phys. Rev. B **93**, 121409(R) (2016).

[62] D. K. Mukherjee, S. Rao, and A. Kundu, Transport through Andreev bound states in a Weyl semimetal quantum dot, Phys. Rev. B **96**, 161408(R) (2017).

[63] S.-B. Zhang, J. Erdmenger, and B. Trauzettel, Chirality Josephson current due to a novel quantum anomaly in inversion-asymmetric Weyl semimetals, Phys. Rev. Lett. **121**, 226604 (2018).

[64] S.-B. Zhang, F. Dolcini, D. Breunig, and B. Trauzettel, Appearance of the universal value e^2/h of the zero-bias conductance in a Weyl semimetal-superconductor junction, Phys. Rev. B **97**, 041116(R) (2018).

[65] R. Saxena, N. Basak, P. Chatterjee, S. Rao, and A. Saha, Thermoelectric properties of inversion symmetry broken Weyl semimetal–Weyl superconductor hybrid junctions, Phys. Rev. B **107**, 195426 (2023).

[66] P. Dutta, F. Parhizgar, and A. M. Black-Schaffer, Finite bulk Josephson currents and chirality blockade removal from interorbital pairing in magnetic Weyl semimetals, Phys. Rev. B **101**, 064514 (2020).

[67] P. Chatterjee and P. Dutta, Quasiparticles-mediated thermal diode effect in Weyl Josephson junctions, arXiv:2312.05008.

[68] U. Khanna, A. Kundu, S. Pradhan, and S. Rao, Proximity-induced superconductivity in Weyl semimetals, Phys. Rev. B **90**, 195430 (2014).

[69] G. Bednik, A. A. Zyuzin, and A. A. Burkov, Superconductivity in Weyl metals, Phys. Rev. B **92**, 035153 (2015).

[70] A. Chen and M. Franz, Superconducting proximity effect and Majorana flat bands at the surface of a Weyl semimetal, Phys. Rev. B **93**, 201105(R) (2016).

[71] P. Baireuther, J. Tworzydlo, M. Breitkreiz, I. Adagideli, and C. W. J. Beenakker, Weyl-Majorana solenoid, New J. Phys. **19**, 025006 (2017).

[72] P. Dutta and A. M. Black-Schaffer, Signature of odd-frequency equal-spin triplet pairing in the Josephson current on the surface of Weyl nodal loop semimetals, Phys. Rev. B **100**, 104511 (2019).

[73] Z. Faraei and S. A. Jafari, Induced superconductivity in Fermi arcs, Phys. Rev. B **100**, 035447 (2019).

[74] Y. Zheng, W. Chen, and D. Y. Xing, Andreev reflection in Fermi-arc surface states of Weyl semimetals, Phys. Rev. B **104**, 075420 (2021).

[75] Y. Baum, E. Berg, S. A. Parameswaran, and A. Stern, Current at a distance and resonant transparency in Weyl semimetals, Phys. Rev. X **5**, 041046 (2015).

[76] K. Pareek and A. Kundu, Quantum transport simulation of nonlocal response in Weyl semimetals, arXiv:1812.05504.

[77] R. Kumari, D. K. Mukherjee, and A. Kundu, Fermi-arcs mediated transport in surface Josephson junctions of Weyl semimetal, arXiv:2401.14956.

[78] A. Kuibarov, O. Suvorov, R. Vocaturo, A. Fedorov, R. Lou, L. Merkwitz, V. Voroshnin, J. I. Facio, K. Koepernik, A. Yaresko, G. Shipunov, S. Aswartham, J. van den Brink, B. Büchner, and S. Borisenko, Evidence of superconducting Fermi arcs, Nature (London) **626**, 294 (2024).

[79] A. Sekine and K. Nomura, Electron correlation induced spontaneous symmetry breaking and Weyl semimetal phase in a strongly spin-orbit coupled system, J. Phys. Soc. Jpn. **82**, 033702 (2013).

[80] W. Qin, L. Li, and Z. Zhang, Chiral topological superconductivity arising from the interplay of geometric phase and electron correlation, Nat. Phys. **15**, 796 (2019).

[81] S. Kourtis, J. Li, Z. Wang, A. Yazdani, and B. A. Bernevig, Universal signatures of Fermi arcs in quasiparticle interference on the surface of Weyl semimetals, Phys. Rev. B **93**, 041109(R) (2016).

[82] S. Datta, *Electronic Transport in Mesoscopic Systems*, Cambridge Studies in Semiconductor Physics and Microelectronic Engineering (Cambridge University Press, 1995).

[83] C. W. Groth, M. Wimmer, A. R. Akhmerov, and X. Waintal, Kwant: A software package for quantum transport, New J. Phys. **16**, 063065 (2014).

[84] G. E. Blonder, M. Tinkham, and T. M. Klapwijk, Transition from metallic to tunneling regimes in superconducting microconstrictions: Excess current, charge imbalance, and supercurrent conversion, Phys. Rev. B **25**, 4515 (1982).

[85] E. Dumitrescu, B. Roberts, S. Tewari, J. D. Sau, and S. Das Sarma, Majorana fermions in chiral topological ferromagnetic nanowires, Phys. Rev. B **91**, 094505 (2015).

[86] T. O. Rosdahl, A. Vuik, M. Kjaergaard, and A. R. Akhmerov, Andreev rectifier: A nonlocal conductance signature of topological phase transitions, Phys. Rev. B **97**, 045421 (2018).

[87] S. Das Sarma, A. Nag, and J. D. Sau, How to infer non-Abelian statistics and topological visibility from tunneling conductance properties of realistic Majorana nanowires, Phys. Rev. B **94**, 035143 (2016).

[88] C. W. J. Beenakker, Quantum transport in semiconductor-superconductor microjunctions, Phys. Rev. B **46**, 12841 (1992).

[89] Y. Takagaki and H. Takayanagi, Quantized conductance in semiconductor-superconductor-junction quantum point contacts, Phys. Rev. B **53**, 14530 (1996).

[90] F. Pientka, G. Kells, A. Romito, P. W. Brouwer, and F. von Oppen, Enhanced zero-bias Majorana peak in the differential tunneling conductance of disordered multisubband quantum-wire/superconductor junctions, Phys. Rev. Lett. **109**, 227006 (2012).

[91] A. De Martino, K. Dorn, F. Buccheri, and R. Egger, Phonon-induced magnetoresistivity of Weyl semimetal nanowires, Phys. Rev. B **104**, 155425 (2021).

[92] J. Xiong, S. K. Kushwaha, T. Liang, J. W. Krizan, M. Hirschberger, W. Wang, R. J. Cava, and N. P. Ong, Evidence for the chiral anomaly in the Dirac semimetal Na_3Bi, Science **350**, 413 (2015).

[93] B.-C. Lin, S. Wang, L.-X. Wang, C.-Z. Li, J.-G. Li, D. Yu, and Z.-M. Liao, Gate-tuned Aharonov-Bohm interference of surface states in a quasiballistic Dirac semimetal nanowire, Phys. Rev. B **95**, 235436 (2017).

[94] L.-X. Wang, C.-Z. Li, D.-P. Yu, and Z.-M. Liao, Aharonov-Bohm oscillations in Dirac semimetal Cd_3As_2 nanowires, Nat. Commun. **7**, 10769 (2016).

[95] M. D. Bachmann, N. Nair, F. Flicker, R. Ilan, T. Meng, N. J. Ghimire, E. D. Bauer, F. Ronning, J. G. Analytis, and P. J. W. Moll, Inducing superconductivity in Weyl semimetal microstructures by selective ion sputtering, Sci. Adv. **3**, e1602983 (2017).